In-situ vertical characteristics of optical properties and heating rates of aerosol over Beijing

Ping Tian[1], Dantong Liu[2*], Delong Zhao[3], Chenjie Yu[4], Quan Liu[1], Mengyu Huang[1], Zhaoze Deng[5], Liang Ran[5], Yunfei Wu[6], Shuo Ding[2], Kang Hu[2], Gang Zhao[7], Chunsheng Zhao[7], Deping Ding[1,3],

1. Beijing Key Laboratory of Cloud, Precipitation and Atmospheric Water Resources, Beijing, 100089, China.

2. Department of Atmospheric Science, School of Earth Sciences, Zhejiang University, Hangzhou, Zhejiang, 310027, China.

3. Field Experiment Base of Cloud and Precipitation Research in North China, China Meteorological Administration, Beijing, 100089,China.

4. Centre for Atmospheric Sciences, School of Earth and Environmental Sciences, University of Manchester, Manchester, M139PL, UK

5. Key Laboratory of Middle Atmosphere and Global Environment Observation, Institute of Atmospheric Physics, Chinese Academy of Sciences, Beijing, 100029, China.

6. CAS Key Laboratory of Regional Climate-Environment for Temperate East Asia, Institute of Atmospheric Physics, Chinese Academy of Sciences, Beijing, 100029, China.

7. Department of Atmospheric and Oceanic Sciences, Peking University, Beijing, 100871, China

Corresponds to: Dantong Liu (dantongliu@zju.edu.cn)

Abstract. Characterizing vertical profiles of aerosol optical properties is important because only replying on the surface or column-integrated measurements is unable to unambiguously constrain the radiative impacts of aerosol. This study presents series of vertical profiles of in-situ measured multi-wavelength optical properties of aerosols during three pollution events in Nov. to Dec. 2016 over Beijing region. For all pollution events, clean periods (CP) before pollution initialization showed higher scattering Ångström exponent and smaller asymmetry parameter (g), and relatively uniform vertical structures. The heavy pollution (HP) periods showed increased particle size, causing these parameters to vary in the opposite way. During the transition periods (TP), regional transport of aged aerosols at upper level was found. The AERONET aerosol optical depth (AOD) matched the in-situ measurements within 10 %, however the AERONET absorption optical depth (AAOD) was 10-20 % higher than in-situ measurements, and this positive discrepancy increased to 30 % at shorter wavelength. The absorption of brown carbon (BrC) was identified by increased absorption Angström exponent (AAE), and the heating rate of black carbon (BC) and BrC was calculated by computing the wavelength-dependent absorption coefficient and actinic flux by the radiative transfer model. BC and BrC had heating rate up to 0.18 K/h and 0.05 K/h in the planetary boundary layer (PBL) respectively during the pollution period. The fraction of BrC absorption increased from 12 % to 40 % in the PBL from CP to HP period. Notably, higher contribution of BrC heating was found above the PBL under polluted condition. This study gives a full picture of shortwave heating impacts of carbonaceous aerosols during different stages of pollution event, and highlights the increased contribution of BrC absorption especially at higher level during pollution.

41

1. Introduction

The optical properties of aerosol, which is how aerosol scatters or absorbs solar radiation, have caused important radiative impacts on earth system (IPCC2013). The optical properties depend on the particle size (Bergin et al., 2001), refractive index (Ebert et al., 2002; Quinn, 2002) and mixing state of aerosols. There are still large uncertainties in evaluating the radiative forcing of aerosol especially in east Asia region due to lack of information on vertical distribution of these parameters (Liao and Seinfeld, 1998; Ramanathan et al., 2001; Li et al., 2017). Previous studies showed that the surface observation or column-integrated measurements may not provide sufficient information to derive vertical profiles of aerosol optical properties (Andrews et al., 2011; Rosati et al., 2016). Modelling studies found the radiative forcing impact is sensitive to the aerosol vertical distribution (Haywood et al., 1998), and especially for the absorbing aerosol such as black carbon (BC) will exert different climatic impacts depending on the location of aerosol layer (Yu et al., 2002; Ban-Weiss et al., 2011; Wilcox et al., 2016). Even though most aerosol was contained inside the planet boundary layer (PBL), the climatic sensitivity to absorbing aerosol rapidly increases with altitude (Ramanathan et al., 2001; Hodnebrog et al., 2014; Nazarenko et al., 2017). Absorbing aerosol above the PBL has the potential to suppress the PBL development and enhance the inversion cap at top of the PBL (Ding et al., 2016; Wang et al., 2018c), further execrating the pollution. However, this impact depends on the location of the absorbing layer which may also promote the convection by heating the layer above (Koch and Del Genio, 2010; Yu et al., 2019). It is therefore important to characterize the vertical profile of absorbing component in the atmosphere in order to understand its influence on atmospheric thermodynamics.

The North China Plain (NCP) has raised great attention in recent decade because of the severe air pollution and high frequency of haze days. The causes of pollution have been widely investigated through surface measurements (Zhang et al., 2013; Zhang et al., 2015; Zhong et al., 2018), however only limited studies have considered the evolution of pollutants in vertical direction (Tian et al., 2019; Wang et al., 2018a). It was found the surface aerosol concentration over Beijing not only depended on the emission but the vertical structure of aerosol distribution was largely dependent on local and synoptic meteorological conditions (Ran et al., 2016a; Zhao et al., 2019), and regional transport will introduce enhanced aerosol

69 loadings to high level (Liu et al., 2018). The vertical distribution of aerosol optical properties, however

70 have not been in detail investigated, which will provide important insights to improve the understanding

71 on the aerosol-PBL interactions hence the causes of pollution (Li et al., 2017).

72 This study chose three typical pollution events occurring in wintertime over Beijing, and performed

73 successive flights on daily basis for each event. The vertical profiles of multi-wavelength aerosol optical

74 properties were in-situ characterized, accounting for all stages during pollution events from pollution

75 starts, full development and cease. The directly measured optical parameters were used as inputs for

76 radiative transfer calculation, hereby the heating rate of light-absorbing aerosols, including black and

77 brown carbon (BrC) was estimated. The results here for the first time provide a full picture of vertical

78 profiles of aerosol optical properties over Beijing region during the heavy pollution events.

79 **2. Instrumentation and data analysis**

80 A Kingair 350ER turbo aircraft in Beijing weather modification office was employed for the in-situ

81 measurements over Beijing during the 2016 winter in this study. Meteorological parameters including the

82 temperature, relative humidity, pressure, wind direction and wind speed with a time resolution of 1 s were

83 measured by the Aircraft Integrated Meteorological Measurement System (AIMMS-20, Aventech

84 Research Inc, Canada), which was calibrated annually. The aerosol instrumentation inside the cabin was

85 connected to an isokinetic inlet (Model:1200, Brechtel Inc, USA), which can deliver particle with a high

86 transport efficiency (90%) for sub-micrometer particles. The maintained room temperature in the cabin

87 had drying effects when the temperature inside was higher than outside the cabin, in addition to which, a

88 silicate direr was utilized ahead of all instruments to maintain the sampling RH lower than 40%.

89 In-situ measurements of aerosol optical properties were performed during three pollution events over

90 Beijing in Nov. 15th to Dec. 21th 2016, including 14 flights covering the start, development and cease

91 stage for each pollution event. All flights were conducted around midday when the PBL was well

92 developed. Table 1 summarizes the information of each flight. The in-cloud data in this study was

93 screened out according to in-situ measured RH and liquid water content, thus only the out-of-cloud data

94 is reported here.

2.1 Aerosol optical properties

The aerosol scattering (σ_{sca}) and hemispheric backscattering (σ_{bsca}) coefficients at λ=450 nm, 525 nm, and 650 nm were measured by an integrating nephelometer (Aurora3000, Ecotech Inc, Australia), and the flowrate of Aurora3000 was maintained at 4 L/min during flight. The baseline of Aurora3000 in real time was corrected for Rayleigh scattering of gas molecule at different air pressure (Fig. S1). In addition, the σ_{sca} and σ_{bsca} at all wavelengths were corrected for truncation affects (Anderson and Ogren, 1998; Müller et al., 2009).

The scattering Ångström exponent (SAE) measures the wavelength dependence of σ_{sca} assuming a power relationship with λ, expressed as:

$$SAE = -\frac{\ln(\sigma_{\lambda 1}/\sigma_{\lambda 2})}{\ln(\lambda_1/\lambda_2)}, \tag{1}$$

where $\sigma_{\lambda 1}$ denotes the σ_{sca} at λ_1, the value of SAE could also be used to reflect particles size with larger particles showing a smaller SAE (Carrico et al., 1998).

The asymmetry parameter (g) is obtained from measured backscattering fraction according to the empirical function from Andrews et al. (2006).

$$g = -7.143889 \cdot \beta^3 + 7.4633439 \cdot \beta^2 - 3.9356 \cdot \beta + 0.9893, \tag{2}$$

where β is the hemi-spherical backscatter fraction ($\sigma_{bsca}/\sigma_{sca}$) measured by the Aurora3000.

The absorbing coefficient (σ_{abs}) at different wavelengths (370, 470, 520, 590, 660, 880, and 950nm) was measured by an Aethalometer (AE33, Magee Scientific Inc, USA) (Hansen, 2005; Drinovec et al., 2015). The flowrate of AE33 was maintained at 4 L/min below 3000 m. The shadowing effect of the AE33 was corrected by the two spot measurements with different attenuation (Drinovec et al., 2017). The multiple scattering artifact of AE33 was corrected by measuring the ambient aerosol in parallel with photoacoustic spectrometer (PASS3, DMT Inc, USA) which is independent of the filter artifacts. The PASS3 was calibrated using the NO_2 and BC standard. (Arnott et al., 2005). Fig. S2 shows the two weeks' ambient measurements between AE33 and PASS3 at three overlapped wavelengths. Multiple scattering correction factor of 2.88 was consistently found at three λ, which was applied to correct the AE33 measurement.

120 The absorbing Ångström exponent (AAE), which can weight the absorption at different wavelength, is

121 calculated using power fitting at seven wavelengths.

122 $\sigma_{abs}(\lambda) = \sigma_{abs,0}(\frac{\lambda}{\lambda_0})^{AAE}$,   (3)

123 We estimated the σ_{abs} of brown carbon (BrC) assuming that BC is the only absorber at λ=950 nm, then

124 the absorption of BC at other wavelengths was extrapolated by assuming an AAE of 1 (Kirchstetter et al.,

125 2004; Lack et al., 2013; Massabò et al., 2015), and the contribution of BrC at each wavelength was

126 obtained by subtracting the BC absorption from the total absorption (Schnaiter et al., 2005;Liu et al.,

127 2015). It should be noted that previous studies point out the AAE_{BC} may be less than 1, thus assuming

128 AAE_{BC}=1 may lead to underestimation of BrC contribution (Gyawali et al., 2009; Lack and Cappa, 2010;

129 Feng et al., 2013). We therefore consider the results reported here is the lower bound of BrC contribution.

130 The single scattering albedo (SSA) is the ratio of the scattering coefficient over the extinction coefficient

131 (σ_{ext}) at a given wavelength.

132 All the data related to volume concentration was corrected for standard temperature and pressure (STP,

133 1013.25hpa , 273.15K). In addition to the aircraft measurements, a micro pulse lidar (MPL, Sigma Inc,

134 USA) was employed to measure the temporal evolution of aerosol extinction vertical profiles, and the

135 vertical wind profile was measured by a wind profile radar with a vertical resolution of 150 m. Column

136 aerosol optical properties during the aircraft observation period were obtained from Aerosol Robotic

137 Network (AERONET) sun-photometer network (Che et al., 2009; Xia et al., 2008), where the site

138 (AERONET BEIJING_PKU) was about 10 km away from the location of vertical profiles.

139 **2.3 Radiative transfer calculation**

140 The atmospheric irradiance and actinic flux are calculated using the pseudo-spherical version of the

141 Discrete Ordinates Radiative Transfer Code (DISORT), as implemented in the libRadtran software

142 package (Emde et al., 2016). The aircraft in-situ measured vertical profiles of AOD, single scattering

143 albedo (SSA) and g are used as inputs. The other input parameters for the radiative transfer calculation is

144 summarized in Table S1. The direct, upward diffuse, and downward diffuse irradiance and actinic flux

145   (AF, in mWm^{-2}) at λ=250-2550 nm are calculated. The spectral instantaneous absorbing power of BC

146   (A_{BC}) or BrC (A_{Brc}) can be calculated by multiplying the absorption coefficient of BC (or BrC) and AF at

147   specified λ, then integrating all λ will obtain the total absorbing power, expressed as:

148    $$A_{BC\ or\ BrC} = \int_{250nm}^{2550nm} AF(\lambda) \cdot \sigma_{BC\ or\ BrC}(\lambda)\, d\lambda, \tag{4}$$

149   By assuming no radiative loss of solar energy and the heat absorbed by aerosol is fully transferred to the

150   surrounding air, the instantaneous heating rate of BC or BrC to ambient air is hence calculated as:

151    $$H_{BC,BrC} = A_{BC,BrC}/(\rho \cdot C_p), \tag{5}$$

152   where ρ and C_P are the air mass density and heat capacity, respectively.

153   **3. Results and discussions**

154   **3.1 Overview and the pollution events**

155   Three pollution events from Nov. 15th to 18th (Case 1), Dec .10th to 12th (Case2), and Dec. 16th to 19th

156   (Case 3) in 2016 were captured. Fig. 1 shows the temporal evolution of surface $PM_{2.5}$, AOD (AAOD)

157   constrained by in-situ aircraft measurements and from AERONET, and vertical profiles of σ_{ext} and wind

158   information during Case 1 pollution event. The other two events are shown in Fig. S3 and Fig. S4. Aircraft

159   vertical profiles were performed on daily basis as the flight time indicated by vertical bars (Fig. 1). Each

160   pollution event was classified as pollution initialization, development and peak pollution periods,

161   corresponding to the pollution levels as clean period (CP, $PM_{2.5,\ surface} < 35\ \mu g/cm^3$), transition period (TP,

162    $35\ \mu g/cm^3 < PM_{2.5,\ surface} < 200\ \mu g/cm^3$) and heavy pollution (HP, $PM_{2.5,\ surface} > 200\ \mu g/cm^3$). For the

163   results here, a total of 14 profiles and 3, 5 and 6 profiles was observed for LP, TP and HP period,

164   respectively (as detailed in Table. 1). As Fig. 1b shows, wind sheer in both wind speed and direction

165   appeared on top of PBL, consistent with the lidar vertical distribution of σ_{ext} (Fig. 1c). During LP, wind

166   profiles (Fig. 1b) showed dominant northwesterly wind with high wind speed throughout the column,

167   enhancing the pollutant dispersion in more developed PBL (Fig. 1c). During TP, the southerly air flow

168   dominated and the $PM_{2.5}$ underwent a rapid increase from 30 to 100 $\mu g\ m^{-3}$ in several hours. During HP,

169   the windspeed was relatively low at all altitude, maintaining the $PM_{2.5}$ at a high level. Some flights

170   experienced boundary cloud (i.e., flight 20161117AM, flight 20161117PM and flight 20161118), which

171   is indicated by the intensive extinction on top of the PBL (Fig. 1c).

172   Fig. 2 summarized the in-situ measured meteorological parameters at different stages of pollution events.

173   The height of PBL (PBLH) was determined by considering a variety of factors. Firstly, a stable potential

174   temperature (θ) (Fig. 2d-f) with vertical gradient $d\theta/dz$ < 5 K/km in the PBL indicated an sufficient

175   convective mixing (Su et al., 2017), with an apparent positive gradient above the PBL indicating a stable

176   layer (Petra Seibert, 2000). Secondly, there is usually a temperature inversion on top of the PBL (Fig. 2a-

177   c). During the CP, the weak temperature inversion (~0.15K/100m) on top of the PBL allowed pollutants

178   to penetrate the PBL and disperse in a higher atmospheric column (Fig. 2b). This inversion was

179   significantly enhanced for the TP and HP periods, to 0.9K/100m and 0.7K/100m respectively. The large

180   increase of the inversion during flight 20161211 was caused by regional transport from the south, when

181   lower-latitude warmer air mass was imposed onto the measurement point (Tian et al., 2019). Additionally,

182   the PBLH decreased gradually as pollution continued during the pollution event, in line with the enhanced

183   aerosol concentration in the PBL. The moisture had similar features that a lower moisture content showed

184   when lower pollution level and vertically efficiently dispersed, whereas stronger inversion also trapped

185   the moisture inside the PBL, leading to a positive vertical gradient with the maximum RH showing on

186   top of the PBL. There were some regional transport influences under TP, resulting in enhanced RH when

187   airmass was advected from the south (Fig. 2f).

3.2 Vertical profile of σ_{ext}, σ_{sca} and σ_{abs}

189   Fig. 3 shows the vertical distribution of aerosol optical properties including extinction (σ_{ext}), scattering

190   (σ_{sca}) and absorbing (σ_{abs}) coefficient. Different structures of vertical profiles were observed for CP, TP

191   and HP periods. During CP, aerosol concentration was low and showed uniform mixing inside the PBL,

192   with the σ_{ext}, σ_{sca} and σ_{abs} ranging from 220-270 Mm^{-1}, 180-240 Mm^{-1}, and 30-50 Mm^{-1}, respectively. The

193   backward trajectories for the CP showed that the air masses were from the northwestern low emission

194   region (Fig. S5). TP showed about 4-fold increase of σ_{ext} compare to the CP. During TP, the σ_{ext}, σ_{sca} and

195   σ_{abs} had large variation inside the PBL, ranging from 325-1435 Mm^{-1}, 300-1275 Mm^{-1}, and 45-160 Mm^{-}

196   ^{1}, respectively, and the mean PBLH decreased to 200-500 m. During these pollution accumulation periods

197 (before the pollution reached peak level), two contrast vertical structures showed. One showed well-
198 mixing in the PBL but declined concentration in the free troposphere (FT) (e.g. flight 20161115PM and
199 20161210) (Fig. 3a). The other one had the increased aerosol layer on top of the PBL, and showed positive
200 vertical gradient for all optical properties at certain level (e.g. flight 20161116 AM, 20161211 and
201 20161216) (Fig. 3b). The former was because of the mostly cleaner northwesterly air mass and higher
202 wind speed influencing the layer above the PBL, while the latter resulted from the southwesterly regional
203 transport (Tian et al., 2019).

204 During HP period, most flights showed consistent exponentially-declined vertical profile patterns, and
205 the PBLH was even lower than that in TP (Fig. 2f). The stronger temperature inversion (Fig. 2c) and lower
206 wind speed (Fig. 1b) inside the PBL led to high stability of the PBL and promoted the pollutant
207 accumulation. The aerosol concentration was largely enhanced towards the surface and sharply declined
208 above the PBL. Interestingly, the absorption showed higher degree of negative vertical gradient than the
209 scattering at λ=440nm, which reflected the different sources and mixing ratios of absorbing and non-
210 absorbing aerosols. The surface emission tends to contain more primary sources of absorbing particles
211 such as BC and BrC, while enhanced secondary aerosol formation at upper level may add additional
212 aerosol extinction.

213 The vertical profiles of σ_{sca} and σ_{abs} during HP can be fitted as:

214 $$\sigma_{sca} = \sigma_{sca,0} \cdot \exp(-a * H) ; \quad a = 0.0012 \pm 0.0001, \tag{6}$$

215 $$\sigma_{abs} = \sigma_{abs,0} \cdot \exp(-b * H) ; \quad b = 0.0015 \pm 0.0001, \tag{7}$$

216 where σ_0 represent the surface value of σ_{sca} and σ_{abs}, and H is the altitude. The a and b are the parameter
217 define the changing rate with the altitude. This parameterization could be used to represent the vertical
218 structure of optical properties under heavy pollution condition.

219 **3.3 Vertical profile of SSA, SAE, AAE and g**

220 Fig. 4 shows the vertical profiles of aerosol single scattering albedo (SSA) for all the flights under
221 different stages of pollution events. Overall, the SSA showed two modes inside the PBL. Under the CP,

222 SSA for most flights was populated at 0.85, and had less variation throughout the column in the PBL.

223 Flight 20161115AM showed a strong elevation of SSA (0.94) at 2200 m (Fig. 4a), which may be

224 influenced by a dust layer (as further discussed in the following). SSA showed positive vertical gradient

225 for the TP and HP inside the PBL, i.e. from the surface to the PBLH, the mean SSA increased from 0.85

226 to 0.91 and from 0.87 to 0.92 for TP and HP period, respectively. This indicates the reduced fraction of

227 absorbing particles, in turn suggesting an enhancement of secondary production of non-absorbing

228 particles. There were a few profiles featuring with large enhancement of SSA (>0.95, for flight 20161211)

229 at high altitude (Fig. 4b), and backtrajectory analysis (Fig. S5) showed that these resulted from regional

230 transport when more aged pollutants were advected to a high altitude. The SSA in the FT was mostly

231 higher than that in the PBL and maintained at 0.9-0.95 for TP and HP, meaning a lower absorbing particle

232 fraction at higher altitude. Comparing among different stages during pollution event, it could be

233 concluded that at the initialization stage of pollution when the total PM was relatively low, a lower SSA

234 exhibited, while the increase of pollution level added more secondary species, hence increasing SSA. This

235 trend consistent with previous ground studies in Beijing (He et al., 2009; Jing et al., 2011).

236 The SAE reflects the particle size with larger size having a smaller SAE. A decreasing SAE was shown

237 for increasing pollution levels inside the PBL (Fig. 4), i.e., from CP to HP, the SAE in the PBL showed

238 an average value of 1.74, 1.45, and 1.21, respectively. For most of the profiles, SAE showed enhancement

239 at higher altitude. This means smaller particle sizes at high level, which may result from a higher

240 scavenging efficiency for larger particles where smaller particle remained un-scavenged in the upper level

241 (Liu et al., 2009). These was exception for flight 20161211, when regional advection transported larger

242 and aged particles to the higher altitude. The particle size also corresponded with asymmetry parameter

243 (g, Fig. 4j-i), with larger particle presents more fraction of forward scattering (larger g).

244 AAE reflects the degree of absorption towards shorter wavelength, such as the presence of BrC will

245 enhance the absorption in the UV. A lower AAE 1.2 ± 0.2 was shown for the CP (Fig. 4g), but increased

246 to 1.56 ± 0.3 for TP in the PBL (Fig. 4h), and additional higher mode of AAE showed at 1.8-2.0 for the

247 HP period (Fig. 4i). There was weak variation of AAE for CP throughout the column, but became largely

248 spreading for TP, i.e., with either positive or negative vertical gradient at different levels. Notably, the

249 AAE showed consistent positive vertical gradient for most of the HP profiles (Fig. 4i). This implied the

250 enhancement of BrC contribution at higher altitude for polluted troposphere. Flight 20161115AM showed

251 a notably increased AAE up to 2 at altitude 2 km (Fig. 4g), which may reflect the influence from dust

252 (Cazorla et al., 2013). The ground AAE had strong seasonal variation with winter normally showing a

253 higher AAE due to higher emissions of solid fuel burning (Sun et al., 2017; Wang et al., 2018b). However,

254 there is still lack of results on the vertical characteristics of AAE due to limited measurements, and the

255 results here highlight the enhancement of BrC at high level, mainly for polluted environment.

3.4 Comparison of column integrated and in-situ constrained AOD/AAOD

257 To compare the AOD and AAOD between AERONET and that constrained by aircraft in-situ

258 measurements, the AERONET data was chosen to match with the aircraft profiles in time (±3h) and

259 location (within 10 km) (the PEK site). The comparison was performed at overlapped wavelength (440nm,

260 675nm, and 870nm) between AERONET and aircraft instruments. As Fig. 5a-c shows, high correlation

261 ($R^2 > 0.95$) was found between columnar and in-situ measurement. In particular, the correlation was most

262 unit under dry condition (RH < 40%), while the AERONET was about 10-20% higher than in-situ

263 measurement when RH >60%. Improved agreement between both may be achieved by considering the

264 particles hygroscopic growth, which requires composition measurement to constrain this factor but this

265 was not available in this study.

266 Fig. 7d-f shows at three wavelengths the AAOD had lower correlations between both methods compare

267 to AOD, with $R^2 = 0.75$, 0.58, and 0.49 at 440 nm, 675 nm, and 870nm, respectively. The columnar AAOD

268 was overall about 10-25 % higher than in-situ measurement. This is consistent with previous findings that

269 the retrieved AAOD from AERONET was biased higher when compared to in-situ measurement

270 (Andrews et al., 2017). Note that there was better agreement during CP, when lower pollution level and

271 lower RH (shown in blue dots). This suggests a lower moisture and less AOD interface may improve the

272 agreement of AAOD. As previous studies pointed out that the retrieval of the AERONET was sensitive to

273 the variation of aerosol vertical distribution (Torres et al., 2014). We speculate that the better agreement

274 for CP was due to the vertically homogeneous distribution of aerosol optical properties, and larger bias

275 for CP and HP periods might be caused by the significant variations of the vertical profiles. Other factors

276 like the particle hygroscopic growth under higher RH may introduce factors in enhancing the absorption,

277 e.g. more lensing effect on BC absorption via thicker and moisture coating (Wu et al., 2017). Though this

278 study is not able to rule out the exact influencing factor in causing this discrepancy, a 25 % overestimation

279 of the AERONET AAOD under polluted condition was shown for the dataset here.

3.5 Heating impacts of BC and BrC

281 Fig. 6 showed vertical profiles of irradiances from radiative transfer calculation using in-situ

282 measurements as model inputs (Table S1). The results show that the presence of aerosols reduced the

283 direct irradiance reaching the surface (Fig. 6a-c) but increased the upward diffuse (Fig. 6d-f) and

284 downward diffuse irradiances, especially above the PBL (Fig. 6g-i). The direct irradiance on the surface

285 ranged from 1×10^9 to 3.5×10^9 mW m^{-2}, with an average of 2.2×10^9 mW m^{-2} during CP (Fig. 6a), which

286 was about two-fold and three-fold larger than that during TP (Fig. 6b) and HP period (Fig. 6c), respectively.

287 The combined direct, diffuse upward and downward irradiance which forms the actinic flux (AF), showed

288 enhancement above the PBL and reduced within the PBL (Fig. 7a-c), but to what extent the enhancement

289 or reduction occurred depends on the aerosol vertical profile. The vertical gradient of AF was slightly

290 modified by aerosol loadings during CP, whereas for the TP and HP, aerosol effects caused AF bout two

291 times smaller within the PBL and 20 % larger above the PBL, leading to an increased vertical gradient of

292 AF.

293 The vertical profiles of absorbing power and heating rate of BC are shown in Fig. 7d-f. The results

294 indicated that the atmospheric heating of BC was mainly inside the PBL for all cases, but exhibited

295 different vertical structure for CP (Fig. 7d), TP (Fig. 7e), and HP period (Fig. 7f). Vertically

296 homogeneously BC heating rates of 0.05 K/h was found inside the PBL during CP (Fig. 7d). During the

297 regional transport cases (flight20161211 and flight20161216) for TP, positive vertical gradient (increase

298 with increasing altitude) of BC heating rates was observed, and as high as 0.1 K/h heating rate could occur

299 at top of the PBL height (Fig. 7e). During the HP period, negative heating rate (decrease with increasing

300 altitude) of BC was found except from one flight on 20161212 in Case 2, and the BC heating rate at the

301 surface could reach as high as 0.15 K/h (Fig. 7f). The reason causing negative vertical gradient of BC

302 heating rate was the higher degree of negative gradient of σ_{abs} (Fig. 3i) than the positive gradient of AF

303 (Fig. 7).

304   The contribution of BrC to absorbing power and heating rates was computed as the integrated portion of

305   absorption over visible wavelength (370–950nm in this study) by subtracting the BC absorption. Fig. 7g-

306   i shows the vertical profile of BrC heating rate. Continuously increase of BrC heating rate in the PBL was

307   observed from CP to HP, with mean heating rate of 0.02 K/h, 0.03 K/h, and 0.05 K/h during CP, TP and

308   HP respectively. Though the BC was the main contributor to the heating in the PBL, the heating of BrC

309   was more evenly distributed and could be comparable with the BC heating rate at high altitude especially

310   during HP period (Fig. 7i).

311   The vertical gradient of the overall heating rate from absorbing components, i.e. increase or decrease

312   heating rate with altitude, will importantly determine the influence on atmospheric stability. If the heating

313   occurred near surface (Case 3), the lower layer will be heated leading to enhanced convective mixing

314   (Sühring et al., 2014;Petaja et al., 2016); whereas if heating above the PBL (Case 2), an increase of

315   temperature inversion will occur hence inhibiting the PBL development trapping the pollutants in the PBL

316   (Wilcox et al., 2016).

317   **3.6 The importance of BrC heating effects**

318   Fig. 8 shows the measured absorption coefficient of BrC and BC inside and above the PBL at different λ

319   for CP, TP and HP period, respectively. The results suggested that both σ_{abs} of BC and BrC increased with

320   the pollution level, e.g. the σ_{abs} at λ= 440nm was 42.8 Mm^{-1} and 7.2 Mm^{-1} on average in the PBL and

321   above the PBL respectively under HP period, and was 4.7 Mm^{-1} and 1.3 Mm^{-1} for LP. The contribution of

322   BrC to total σ_{abs} was found to increase from CP to HP period (Fig. 8c, f). This is in line with previous

323   studies in urban Beijing that more BrC contribution to total absorption was found under higher pollution

324   level (Xie et al., 2019;Ran et al., 2016b), suggesting the important role of BrC on absorption under

325   polluted condition.

326   The BrC contribution to total heating rate showed notably different vertical structures. During CP, all

327   profiles showed consistently low BrC contribution throughout the column, with about 7 % at the surface

328   and 9 % in the FT (Fig. 8g). This means the low primary emission or the emission after being diluted by

329   clean air mass had not contained important fraction of absorbing organics. During TP, BrC contribution

330   inside the PBL increased to 22 % and showed considerable variation at higher level (Fig. 8h). During HP

331   period, the surface contribution was comparable with that in TP, but showed remarkably enhanced BrC

332   heating contribution at higher altitude, with a vertically increasing rate of 1.5 %/m in the PBL and reached

333   as high as 45 % in the LFT. The higher heating contribution of BrC at higher altitude means the BrC

334   absorption played an important role in heating at upper level, which may enhance the temperature

335   inversion at the level hereby inhibiting the convective mixing under the heated layer.

336   By comparing the BrC heating contribution at the surface, there was an increase from CP to TP, however,

337   not from TP to HP. This suggests the primary emission will increase the BrC fraction from CP to TP, but

338   for even more pollution environment from TP to HP, the primary emission may provide limited further

339   increased faction of BrC. The primary BrC may result from a range of combustion sources, with the

340   polluted region at the south of Beijing may contain higher fraction of residential coal burning sources

341   (Sun et al., 2017;Xie et al., 2019) which may influence the Beijing region under polluted period. The

342   relatively consistent BrC contribution at ~20 % from TP to HP suggested the relatively uniform BrC

343   profiles for the primary sources. During TP, the BrC contribution above the PBL had rarely been above

344   30 % (Fig. 8h), however during HP, there was further enhancement of BrC contribution up to 45 % above

345   the PBL (Fig. 8i). Note that there was no direct injection of biomass burning plume to the high altitude

346   during the study period, the higher portion of BrC absorption above the PBL during HP may be formed

347   through secondary production in addition to the primary source contribution. As Fig. 7a-c shows, there

348   was more intensive actinic flux received at higher altitude and this will promote the photochemical

349   reactions of gas-phase species, allowing more secondary formation of aerosol which may contain a

350   fraction of BrC (Feng et al., 2013;Nakayama et al., 2013). Previous studies also found promoted BrC

351   formation with light source under certain RH (Nguyen et al., 2012; Updyke et al., 2012; Laskin et al.,

352   2015; Zhao et al., 2015). The positive gradient of BrC heating contribution more likely resulted from

353   enhanced RH from the surface to the top of PBL (Fig. 2i), because increased moisture will promote the

354   aqueous reaction and gas-to-aerosol conversion which may also form part of the BrC observed here

355   (Ervens et al., 2011; Nakayama et al., 2013). The secondary formation of BrC also requires the inorganic

356   or VOC precursors being transported to the high level, therefore the enhancement of BrC mostly occurred

357   under higher pollution level when sufficient gas precursors was transport to the level. The BrC may be

358 also subject to bleaching process and lose the absorbance (Sareen et al., 2013; Lee et al., 2014; Wong et

359 al., 2019), because the profiles in this study were conducted over an urban megacity where the sampled

360 pollutants were fairly young and may have not experienced sufficient ageing time for BrC to be degraded.

4. Conclusions

362 This study provides detailed characterization of vertical profiles of aerosol optical properties over the

363 Beijing region by continuous aircraft in-situ measurements at different stages during the pollution events.

364 The results combining the direct measurements of scattering and absorption at multiple wavelength, give

365 a full picture of how the optical properties had evolved at different layers during typical pollution event.

366 During clean period for pollution initialization (CP), the aerosols showed relatively uniform

367 characteristics throughout the planetary boundary layer (PBL) and lower free troposphere (FT), such as

368 lowing scattering or absorption coefficient, larger SAE (due to smaller particle size) and lower fraction

369 of brown carbon (BrC) reflected by smaller AAE. The transition period (TP) when pollution was

370 developing had large variation of all optical properties, and enhanced aerosol loadings at higher altitude

371 were encountered when being influenced by regional advection. The fully developed heavy pollution

372 period (HP) featured with the shallow PBL accumulated over 80 % of the scattering and absorption within

373 the PBL, and deceased SAE due to enlarged particles size. Notably the absorption towards shorter

374 wavelength became larger under more polluted environment, especially for the higher altitude.

375 The AOD and AAOD measured by passive remote sensing was for the first time compared with in-situ

376 measurements over this polluted region. AOD showed high correlation between AERONET and in-situ

377 measurement within 10 %, and the most discrepancy between both could be possibly resolved by

378 considering the hygroscopic growth of aerosols under high RH condition. The AAOD however showed

379 10-25 % higher for remote sensing especially at shorter wavelength, consistent with other studies(Müller

380 et al., 2012;Andrews et al., 2017). The possibilities of causing this could be the non-homogeneously

381 vertically structure of optical properties, mixing state of light-absorbing aerosol, and also the particle

382 hygroscopic growth, which are unable to be ruled out only using the results here.

383 The heating rates of aerosols was calculated by the radiative transfer model (DISORT) by using in-situ

384 measured profiles as inputs. BC was the main heating species, having 0.05 K/h, 0.1 K/h and 0.15 K/h

385 heating rate in the PBL during pollution initialization, transition and full development respectively, and

386 showed positive vertical gradient of heating when regional transport The contribution of BrC was found

387 to increase by 20 % throughout the column from CP to HP period, in particular the increased BrC

388 contribution was pronounced at the layer above the PBL during HP, which was proposed to result from

389 the intensive photochemical reactions above the PBL. The BrC present at this layer will have the potential

390 to contribute to the heating at this layer, hence enhancing the temperature inversion on top of the PBL

391 hereby the capping effect to the pollutants trapped in the PBL. Particles at higher altitude may be

392 transported to wider region spatially in both vertical and horizontal directions through convection, which

393 may lead BrC present at this layer to have wilder and longer radiative impacts. Different mechanism of

394 BrC formation at different levels such as above the PBL (where more solar flux received) or within the

395 PBL (where more moisture was constrained) warrants future studies.

396

397 **Data availability.** All data in this paper are available from the authors upon request

398 (tianping@bj.cma.gov.cn).

399 **Competing interests.** The authors declare no conflicts of interest.

400 **Author contribution.** D. D., and M. H. led and designed the study; P. T. and D. L. designed the study,

401 set up the experiment, analyzed the data, and wrote the paper. D. Z. and Q. L. conducted the aircraft

402 observation. C. Y. performed the radiative transfer model calculation. Z.D., L. R., and Y. W. contributed

403 to the aircraft data analysis. S.D and K. H contribute to the surface data analysis. G. Z and C. Z. conducted

404 the aerosol absorption comparison experiment.

405 **Acknowledgment.** This research was supported by the National key Research and Development Program

406 of China (2016YFA0602001), and the National Natural Science Foundation of China (41875044,

407 41675038, 41875167). Part of this work is supported by the National Center of Meteorology, Abu Dhabi,

408 UAE under the UAE Research Program for Rain Enhancement Science.

409

Reference

Anderson, T. L., and Ogren, J. A.: Determining Aerosol Radiative Properties Using the TSI 3563 Integrating Nephelometer, Aerosol Sci. Technol., 29, 57-69, 10.1080/02786829808965551, 1998.

Andrews, E., Sheridan, P. J., Fiebig, M., McComiskey, A., Ogren, J. A., Arnott, P., Covert, D., Elleman, R., Gasparini, R., Collins, D., Jonsson, H., Schmid, B., and Wang, J.: Comparison of methods for deriving aerosol asymmetry parameter, J. Geophys. Res., 111, 10.1029/2004jd005734, 2006.

Andrews, E., Sheridan, P. J., and Ogren, J. A.: Seasonal differences in the vertical profiles of aerosol optical properties over rural Oklahoma, Atmos. Chem. Phys., 11, 10661-10676, 10.5194/acp-11-10661-2011, 2011.

Andrews, E., Ogren, J. A., Kinne, S., and Samset, B.: Comparison of AOD, AAOD and column single scattering albedo from AERONET retrievals and in situ profiling measurements, Atmos. Chem. Phys., 17, 6041-6072, 10.5194/acp-17-6041-2017, 2017.

Arnott, W. P., Hamasha, K., Moosmüller, H., Sheridan, P. J., and Ogren, J. A.: Towards Aerosol Light-Absorption Measurements with a 7-Wavelength Aethalometer: Evaluation with a Photoacoustic Instrument and 3-Wavelength Nephelometer, Aerosol Sci. Technol., 39, 17-29, 10.1080/027868290901972, 2005.

Ban-Weiss, G. A., Cao, L., Bala, G., and Caldeira, K.: Dependence of climate forcing and response on the altitude of black carbon aerosols, Clim. Dynam., 38, 897-911, 10.1007/s00382-011-1052-y, 2011.

Bergin, M. H., Cass, G. R., Xu, J., Fang, C., Zeng, L. M., Yu, T., Salmon, L. G., Kiang, C. S., Tang, X. Y., Zhang, Y. H., and Chameides, W. L.: Aerosol radiative, physical, and chemical properties in Beijing during June 1999, J. Geophys. Res., 106, 17969-17980, Doi 10.1029/2001jd900073, 2001.

Carrico, C. M., Rood, M. J., and Ogren, J. A.: Aerosol light scattering properties at Cape Grim, Tasmania, during the First Aerosol Characterization Experiment (ACE 1), J. Geophys. Res., 103, 16565, 10.1029/98jd00685, 1998.

Cazorla, A., Bahadur, R., Suski, K. J., Cahill, J. F., Chand, D., Schmid, B., Ramanathan, V., and Prather, K. A.: Relating aerosol absorption due to soot, organic carbon, and dust to emission sources determined from in-situ chemical measurements, Atmos. Chem. Phys., 13, 9337-9350, 10.5194/acp-13-9337-2013, 2013.

Che, H., Zhang, X., Chen, H., Damiri, B., Goloub, P., Li, Z., Zhang, X., Wei, Y., Zhou, H., Dong, F., Li, D., and Zhou, T.: Instrument calibration and aerosol optical depth validation of the China Aerosol Remote Sensing Network, J. Geophys. Res., 114, 10.1029/2008jd011030, 2009.

Ding, A. J., Huang, X., Nie, W., Sun, J. N., Kerminen, V. M., Petäjä, T., Su, H., Cheng, Y. F., Yang, X. Q., Wang, M. H., Chi, X. G., Wang, J. P., Virkkula, A., Guo, W. D., Yuan, J., Wang, S. Y., Zhang, R. J., Wu, Y. F., Song, Y., Zhu, T., Zilitinkevich, S., Kulmala, M., and Fu, C. B.: Enhanced haze pollution by black carbon in megacities in China, Geophys. Res. Lett., 43, 2873-2879, 10.1002/2016gl067745, 2016.

Drinovec, L., Močnik, G., Zotter, P., Prévôt, A. S. H., Ruckstuhl, C., Coz, E., Rupakheti, M., Sciare, J., Müller, T., Wiedensohler, A., and Hansen, A. D. A.: The "dual-spot" Aethalometer: an improved measurement of aerosol black carbon with real-time loading compensation, Atmos. Meas. Tech., 8, 1965–1979, https://doi.org/10.5194/amt-8-1965-2015, 2015.

Drinovec, L., Gregorič, A., Zotter, P., Wolf, R., Bruns, E. A., Prévôt, A. S. H., Petit, J.-E., Favez, O., Sciare, J., Arnold, I. J., Chakrabarty, R. K., Moosmüller, H., Filep, A., and Močnik, G.: The filter-loading effect by ambient aerosols in filter absorption photometers depends on the coating of the sampled particles, Atmos. Meas. Tech., 10, 1043-1059, 10.5194/amt-10-1043-2017, 2017.

Ebert, M., Weinbruch, S., Rausch, A., Gorzawski, G., Helas, G., Hoffmann, P., and Wex, H.: Complex refractive index of aerosols during LACE 98 as derived from the analysis of individual particles, J. Geophys. Res. Atmos., 107, LAC 3-1-LAC 3-15, 10.1029/2000jd000195, 2002.

Emde, C., Buras-Schnell, R., Kylling, A., Mayer, B., Gasteiger, J., Hamann, U., Kylling, J., Richter, B., Pause, C., Dowling, T., and Bugliaro, L.: The libRadtran software package for radiative transfer calculations (version 2.0.1), Geosci. Model Dev., 9, 1647-1672, 10.5194/gmd-9-1647-2016, 2016.

Ervens, B., Turpin, B. J., and Weber, R. J.: Secondary organic aerosol formation in cloud droplets and aqueous particles (aqSOA): a review of laboratory, field and model studies, Atmos. Chem. Phys., 11, 11069-11102, 10.5194/acp-11-11069-2011, 2011.

Feng, Y., Ramanathan, V., and Kotamarthi, V. R.: Brown carbon: a significant atmospheric absorber of solar radiation?, Atmos. Chem. Phys., 13, 8607-8621, 10.5194/acp-13-8607-2013, 2013.

Gyawali, M., Arnott, W. P., and Moosmuller, H.: In situ aerosol optics in Reno, NV, USA, during and after the summer 2008 California wildfires and the influence of absorbing and non-absorbing organic

coatings on spectral light absorption, Atmos. Chem. Phys., 9, 8009-8015, 2009.

Hansen, A. D. A.: The Aethalometer Manual, Berkeley, California, USA, pp., 2005.

Haywood, J. M., Schwarzkopf, M. D., and Ramaswamy, V.: Estimates of radiative forcing due to modeled increases in tropospheric ozone, J. Geophys. Res. Atmos., 103, 16999-17007, 10.1029/98jd01348, 1998.

He, X., Li, C. C., Lau, A. K. H., Deng, Z. Z., Mao, J. T., Wang, M. H., and Liu, X. Y.: An intensive study of aerosol optical properties in Beijing urban area, Atmos. Chem. Phys., 9, 8903-8915, 2009.

Hodnebrog, O., Myhre, G., and Samset, B. H.: How shorter black carbon lifetime alters its climate effect, Nat. Commun., 5, 1-7, 10.1038/ncomms6065, 2014.

Jing, J. S., Zhang, R. J., Tao, J., and Zhang, L. M.: Observations of Aerosol Optical Properties in the Beijing Urban Area inSummer, Atmos. Sci. Lett., 4, 338-343, 2011.

Kirchstetter, T. W., Novakov, T., and Hobbs, P. V.: Evidence that the spectral dependence of light absorption by aerosols is affected by organic carbon, J. Geophys. Res. Atmos., 109, n/a-n/a, 10.1029/2004jd004999, 2004.

Koch, D., and Del Genio, A. D.: Black carbon semi-direct effects on cloud cover: review and synthesis, Atmos. Chem. Phys., 10, 7685-7696, 10.5194/acp-10-7685-2010, 2010.

Lack, D. A., and Cappa, C. D.: Impact of brown and clear carbon on light absorption enhancement, single scatter albedo and absorption wavelength dependence of black carbon, Atmos. Chem. Phys., 10, 4207-4220, 10.5194/acp-10-4207-2010, 2010.

Lack, D. A., Bahreni, R., Langridge, J. M., Gilman, J. B., and Middlebrook, A. M.: Brown carbon absorption linked to organic mass tracers in biomass burning particles, Atmos. Chem. Phys., 13, 2415-2422, 10.5194/acp-13-2415-2013, 2013.

Laskin, A., Laskin, J., and Nizkorodov, S. A.: Chemistry of atmospheric brown carbon, Chemical reviews, 115, 4335-4382, 10.1021/cr5006167, 2015.

Lee, H. J., Aiona, P. K., Laskin, A., Laskin, J., and Nizkorodov, S. A.: Effect of solar radiation on the optical properties and molecular composition of laboratory proxies of atmospheric brown carbon, Environ. Sci. Technol., 48, 10217-10226, 10.1021/es502515r, 2014.

Li, Z., Guo, J., Ding, A., Liao, H., Liu, J., Sun, Y., Wang, T., Xue, H., Zhang, H., and Zhu, B.: Aerosol and boundary-layer interactions and impact on air quality, National Science Review, 4, 810-833,

494   10.1093/nsr/nwx117, 2017.

495   Liao, H., and Seinfeld, J. H.: Radiative forcing by mineral dust aerosols: Sensitivity to key variables, J.

496   Geophys. Res. Atmos., 103, 31637-31645, 10.1029/1998jd200036, 1998.

497   Liu, D., Taylor, J. W., Young, D. E., Flynn, M. J., Coe, H., and Allan, J. D.: The effect of complex black

498   carbon microphysics on the determination of the optical properties of brown carbon, Geophys. Res. Lett.,

499   42, 613-619, 10.1002/2014gl062443, 2015.

500   Liu, P., Zhao, C., Liu, P., Deng, Z., Huang, M., Ma, X., and Tie, X.: Aircraft study of aerosol vertical

501   distributions over Beijing and their optical properties, Tellus B: Chemical and Physical Meteorology, 61,

502   756-767, 10.1111/j.1600-0889.2009.00440.x, 2009.

503   Liu, Q., Ding, D., Huang, M., Tian, P., Zhao, D., Wang, F., Li, X., Bi, K., Sheng, J., Zhou, W., Liu, D.,

504   Huang, R., and Zhao, C.: A study of elevated pollution layer over the North China Plain using aircraft

505   measurements, Atmos. Environ., 190, 188-194, 10.1016/j.atmosenv.2018.07.024, 2018.

506   Müller, D., Lee, K. H., Gasteiger, J., Tesche, M., Weinzierl, B., Kandler, K., Müller, T., Toledano, C., Otto,

507   S., Althausen, D., and Ansmann, A.: Comparison of optical and microphysical properties of pure Saharan

508   mineral dust observed with AERONET Sun photometer, Raman lidar, and in situ instruments during

509   SAMUM 2006, J. Geophys. Res. Atmos., 117, n/a-n/a, 10.1029/2011jd016825, 2012.

510   Müller, T., Nowak, A., Wiedensohler, A., Sheridan, P., Laborde, M., Covert, D. S., Marinoni, A., Imre, K.,

511   Henzing, B., Roger, J.-C., dos Santos, S. M., Wilhelm, R., Wang, Y.-Q., and de Leeuw, G.: Angular

512   Illumination and Truncation of Three Different Integrating Nephelometers: Implications for Empirical,

513   Size-Based Corrections, Aerosol Sci. Technol., 43, 581-586, 10.1080/02786820902798484, 2009.

514   Massabò, D., Caponi, L., Bernardoni, V., Bove, M. C., Brotto, P., Calzolai, G., Cassola, F., Chiari, M.,

515   Fedi, M. E., Fermo, P., Giannoni, M., Lucarelli, F., Nava, S., Piazzalunga, A., Valli, G., Vecchi, R., and

516   Prati, P.: Multi-wavelength optical determination of black and brown carbon in atmospheric aerosols,

517   Atmos. Environ., 108, 1-12, 10.1016/j.atmosenv.2015.02.058, 2015.

518   Nakayama, T., Sato, K., Matsumi, Y., Imamura, T., Yamazaki, A., and Uchiyama, A.: Wavelength and

519   NOx dependent complex refractive index of SOAs generated from the photooxidation of toluene, Atmos.

520   Chem. Phys., 13, 531-545, 10.5194/acp-13-531-2013, 2013.

521   Nazarenko, L., Rind, D., Tsigaridis, K., Del Genio, A. D., Kelley, M., and Tausnev, N.: Interactive nature

of climate change and aerosol forcing, J. Geophys. Res. Atmos., 122, 3457-3480, 10.1002/2016jd025809, 2017.

Nguyen, T. B., Lee, P. B., Updyke, K. M., Bones, D. L., Laskin, J., Laskin, A., and Nizkorodov, S. A.: Formation of nitrogen- and sulfur-containing light-absorbing compounds accelerated by evaporation of water from secondary organic aerosols, J. Geophys. Res. Atmos., 117, n/a-n/a, 10.1029/2011jd016944, 2012.

Petaja, T., Jarvi, L., Kerminen, V. M., Ding, A. J., Sun, J. N., Nie, W., Kujansuu, J., Virkkula, A., Yang, X. Q., Fu, C. B., Zilitinkevich, S., and Kulmala, M.: Enhanced air pollution via aerosol-boundary layer feedback in China, Sci. Repts., 6, 18998, 10.1038/srep18998, 2016.

Petra Seibert, F. B., Sven-Erik Gryning, Sylvain Joffre, Alix Rasmussen, Philippe Tercier: Review and intercomparison of operational methods for the determination of the mixing height, Atmos. Environ., 34, 27, 2000.

Quinn, P. K.: Aerosol optical properties during INDOEX 1999: Means, variability, and controlling factors, J. Geophys. Res., 107, 10.1029/2000jd000037, 2002.

Ramanathan, V., Crutzen, P. J., Kiehl, J. T., and Rosenfeld, D.: Aerosols, climate, and the hydrological cycle, Science, 294, 2119-2124, 10.1126/science.1064034, 2001.

Ran, L., Deng, Z., Xu, X., Yan, P., Lin, W., Wang, Y., Tian, P., Wang, P., Pan, W., and Lu, D.: Vertical profiles of black carbon measured by a micro-aethalometer in summer in the North China Plain, Atmos. Chem. Phys., 16, 10441-10454, 10.5194/acp-16-10441-2016, 2016a.

Ran, L., Deng, Z. Z., Wang, P. C., and Xia, X. A.: Black carbon and wavelength-dependent aerosol absorption in the North China Plain based on two-year aethalometer measurements, Atmos. Environ., 142, 132-144, 10.1016/j.atmosenv.2016.07.014, 2016b.

Rosati, B., Herrmann, E., Bucci, S., Fierli, F., Cairo, F., Gysel, M., Tillmann, R., Größ, J., Gobbi, G. P., Di Liberto, L., Di Donfrancesco, G., Wiedensohler, A., Weingartner, E., Virtanen, A., Mentel, T. F., and Baltensperger, U.: Studying the vertical aerosol extinction coefficient by comparing in situ airborne data and elastic backscatter lidar, Atmos. Chem. Phys., 16, 4539-4554, 10.5194/acp-16-4539-2016, 2016.

Sühring, M., Maronga, B., Herbort, F., and Raasch, S.: On the Effect of Surface Heat-Flux Heterogeneities on the Mixed-Layer-Top Entrainment, Boundary-Layer Meteorol., 151, 531-556, 10.1007/s10546-014-

9913-7, 2014.

Sareen, N., Moussa, S. G., and McNeill, V. F.: Photochemical aging of light-absorbing secondary organic aerosol material, The journal of physical chemistry. A, 117, 2987-2996, 10.1021/jp309413j, 2013.

Schnaiter, M., Schmid, O., Petzold, A., Fritzsche, L., Klein, K. F., Andreae, M. O., Helas, G., Thielmann, A., Gimmler, M., Möhler, O., Linke, C., and Schurath, U.: Measurement of Wavelength-Resolved Light Absorption by Aerosols Utilizing a UV-VIS Extinction Cell, Aerosol Sci. Technol., 39, 249-260, 10.1080/027868290925958, 2005.

Su, T., Li, J., Li, C., Xiang, P., Lau, A. K.-H., Guo, J., Yang, D., and Miao, Y.: An intercomparison of long-term planetary boundary layer heights retrieved from CALIPSO, ground-based lidar, and radiosonde measurements over Hong Kong, J. Geophys. Res. Atmos., 122, 3929-3943, 10.1002/2016jd025937, 2017.

Sun, J., Zhi, G., Hitzenberger, R., Chen, Y., Tian, C., Zhang, Y., Feng, Y., Cheng, M., Zhang, Y., Cai, J., Chen, F., Qiu, Y., Jiang, Z., Li, J., Zhang, G., and Mo, Y.: Emission factors and light absorption properties of brown carbon from household coal combustion in China, Atmos. Chem. Phys., 17, 4769-4780, 10.5194/acp-17-4769-2017, 2017.

Tian, P., Liu, D., Huang, M., Liu, Q., Zhao, D., Ran, L., Deng, Z., Wu, Y., Fu, S., Bi, K., Gao, Q., He, H., Xue, H., and Ding, D.: The evolution of an aerosol event observed from aircraft in Beijing: An insight into regional pollution transport, Atmos. Environ., 206, 11-20, 10.1016/j.atmosenv.2019.02.005, 2019.

Torres, B., Dubovik, O., Toledano, C., Berjon, A., Cachorro, V. E., Lapyonok, T., Litvinov, P., and Goloub, P.: Sensitivity of aerosol retrieval to geometrical configuration of ground-based sun/sky radiometer observations, Atmos. Chem. Phys., 14, 847-875, 10.5194/acp-14-847-2014, 2014.

Updyke, K. M., Nguyen, T. B., and Nizkorodov, S. A.: Formation of brown carbon via reactions of ammonia with secondary organic aerosols from biogenic and anthropogenic precursors, Atmos. Environ., 63, 22-31, 10.1016/j.atmosenv.2012.09.012, 2012.

Wang, F., Li, Z., Ren, X., Jiang, Q., He, H., Dickerson, R. R., Dong, X., and Lv, F.: Vertical distributions of aerosol optical properties during the spring 2016 ARIAs airborne campaign in the North China Plain, Atmos. Chem. Phys., 18, 8995-9010, 10.5194/acp-18-8995-2018, 2018a.

Wang, J., Nie, W., Cheng, Y., Shen, Y., Chi, X., Wang, J., Huang, X., Xie, Y., Sun, P., Xu, Z., Qi, X., Su, H., and Ding, A.: Light absorption of brown carbon in eastern China based on 3-year multi-wavelength

aerosol optical property observations and an improved absorption Ångström exponent segregation method, Atmos. Chem. Phys., 18, 9061-9074, 10.5194/acp-18-9061-2018, 2018b.

Wang, Z., Huang, X., and Ding, A.: Dome effect of black carbon and its key influencing factors: a one-dimensional modelling study, Atmos. Chem. Phys., 18, 2821-2834, 10.5194/acp-18-2821-2018, 2018c.

Wilcox, E. M., Thomas, R. M., Praveen, P. S., Pistone, K., Bender, F. A., and Ramanathan, V.: Black carbon solar absorption suppresses turbulence in the atmospheric boundary layer, Proc. Natl. Acad. Sci. USA., 113, 11794-11799, 10.1073/pnas.1525746113, 2016.

Wong, J. P. S., Tsagkaraki, M., Tsiodra, I., Mihalopoulos, N., Violaki, K., Kanakidou, M., Sciare, J., Nenes, A., and Weber, R. J.: Atmospheric evolution of molecular-weight-separated brown carbon from biomass burning, Atmos. Chem. Phys., 19, 7319-7334, 10.5194/acp-19-7319-2019, 2019.

Wu, Y., Wang, X., Tao, J., Huang, R., Tian, P., Cao, J., Zhang, L., Ho, K.-F., Han, Z., and Zhang, R.: Size distribution and source of black carbon aerosol in urban Beijing during winter haze episodes, Atmos. Chem. Phys., 17, 7965-7975, 10.5194/acp-17-7965-2017, 2017.

Xia, X., Eck, T. F., Holben, B. N., Phillippe, G., and Chen, H.: Analysis of the weekly cycle of aerosol optical depth using AERONET and MODIS data, J. Geophys. Res., 113, 10.1029/2007jd009604, 2008.

Xie, C., Xu, W., Wang, J., Wang, Q., Liu, D., Tang, G., Chen, P., Du, W., Zhao, J., Zhang, Y., Zhou, W., Han, T., Bian, Q., Li, J., Fu, P., Wang, Z., Ge, X., Allan, J., Coe, H., and Sun, Y.: Vertical characterization of aerosol optical properties and brown carbon in winter in urban Beijing, China, Atmos. Chem. Phys., 19, 165-179, 10.5194/acp-19-165-2019, 2019.

Yu, H., Liu, S. C., and Dickinson, R. E.: Radiative effects of aerosols on the evolution of the atmospheric boundary layer, J. Geophys. Res., 107, 10.1029/2001jd000754, 2002.

Yu, P. F., Toon, O. B., Bardeen, C. G., Zhu, Y. Q., Rosenlof, K. H., Portmann, R. W., Thornberry, T. D., Gao, R. S., SDavis, S. M., Wolf, E. T., Gouw, J. D., Peterson, D. A., Fromm, M. D., and Robock, A.: Black carbon lofts wildfire smoke high into the stratosphere to form a persistent plume, Science, 365, 14, 2019.

Zhang, R., Jing, J., Tao, J., Hsu, S. C., Wang, G., Cao, J., Lee, C. S. L., Zhu, L., Chen, Z., Zhao, Y., and Shen, Z.: Chemical characterization and source apportionment of PM2.5 in Beijing: seasonal perspective, Atmos. Chem. Phys., 13, 7053-7074, 10.5194/acp-13-7053-2013, 2013.

Zhang, X. Y., Wang, J. Z., Wang, Y. Q., Liu, H. L., Sun, J. Y., and Zhang, Y. M.: Changes in chemical components of aerosol particles in different haze regions in China from 2006 to 2013 and contribution of meteorological factors, Atmos. Chem. Phys., 15, 12935-12952, 10.5194/acp-15-12935-2015, 2015.

Zhao, D. L., Huang, M. Y., Tian, P., He, H., Lowe, D., Zhou, W., Sheng, J. J., Wang, F., Bi, K., Kong, S. F., Yang, Y., Liu, Q., Liu, D. T., and Ding, D. P.: Vertical characteristics of black carbon physical properties over Beijing region in warm and cold seasons, Atmos. Environ., 213, 296-310, 2019.

Zhao, R., Lee, A. K. Y., Huang, L., Li, X., Yang, F., and Abbatt, J. P. D.: Photochemical processing of aqueous atmospheric brown carbon, Atmos. Chem. Phys., 15, 6087-6100, 10.5194/acp-15-6087-2015, 2015.

Zhong, J., Zhang, X., Dong, Y., Wang, Y., Liu, C., Wang, J., Zhang, Y., and Che, H.: Feedback effects of boundary-layer meteorological factors on cumulative explosive growth of PM_{2.5} during winter heavy pollution episodes in Beijing from 2013 to 2016, Atmos. Chem. Phys., 18, 247-258, 10.5194/acp-18-247-2018, 2018.

634

635

636

637

638   Table 1. Flight summary of the vertical observation of aerosol optical properties campaign

Flight number	Time range Local time	Case	Pollution period	Mixing layer height
RF1	20161115 12:00	Case_1	LP	1450 m
RF2	20161115 14:00	Case_1	LP	1450 m
RF3	20161116 12:00	Case_1	TP	850 m
RF4	20161116 14:00	Case_1	TP	750 m
RF5	20161117 12:00	Case_1	TP	1250 m
RF6	20161117 14:00	Case_1	TP	1150 m
RF7	20161118 12:00	Case_1	HP	1050 m
RF8	20161210 14:00	Case_2	LP	950 m
RF9	20161211 14:00	Case_2	MP	950 m
RF10	20161212 14:00	Case_2	HP	450 m
RF11	20161216 14:00	Case_3	TP	350 m
RF12	20161217 14:00	Case_3	HP	350 m
RF13	20161218 14:00	Case_3	HP	350 m
RF14	20161219 14:00	Case_3	HP	250 m

639
640
641
642
643
644
645
646
647
648
649

650
651
652
653

654
655
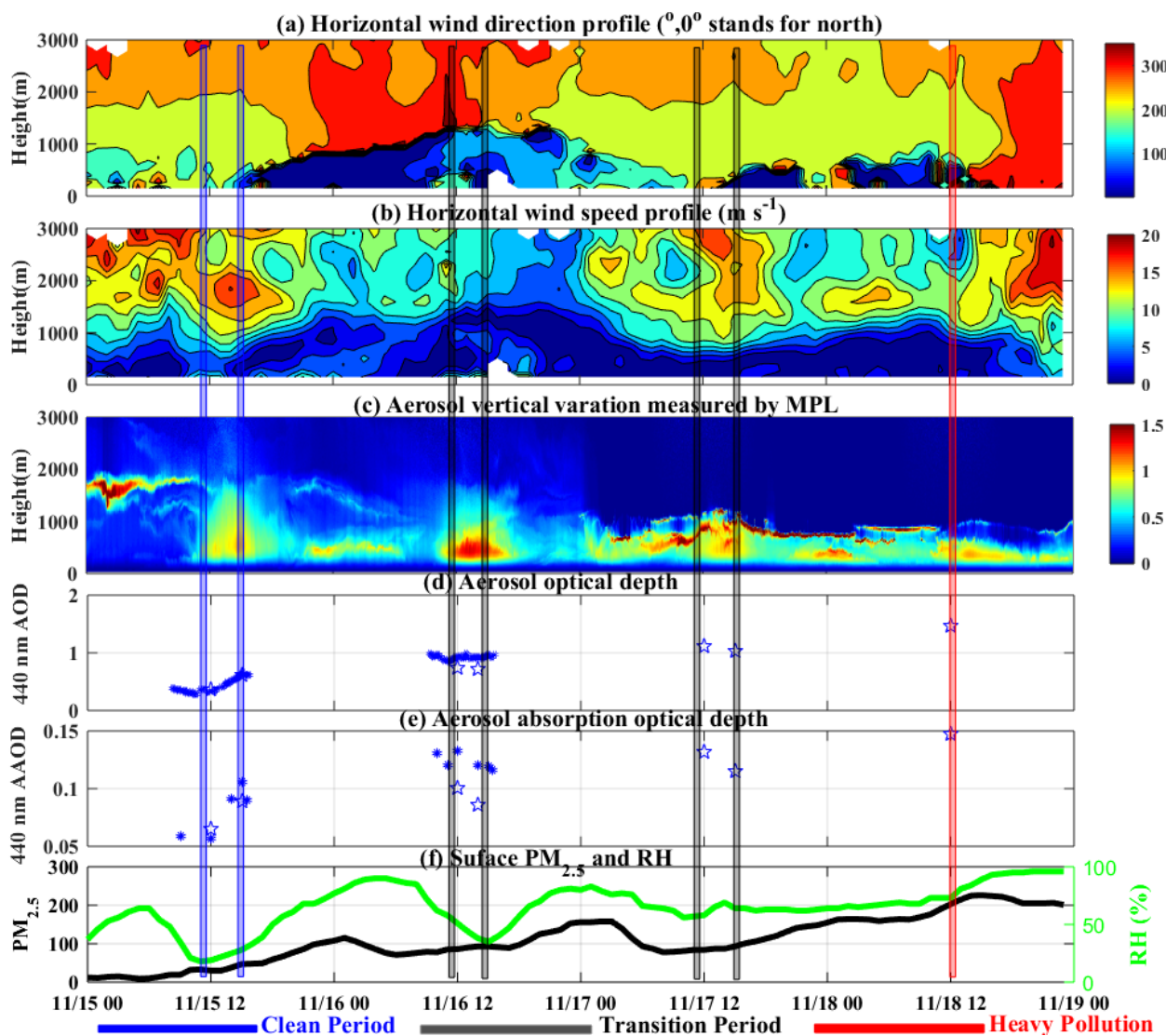
Fig. 1. Temporal variations from Nov. 15th to 18th of vertical profiles of wind direction (a), and wind speed (b) measured by wind profile radar,; (c) particle extinction measured by MPL lidar;) aerosol optical depth (d) and aerosol absorption optical depth (e) from AERONET (asterisk) and derived from aircraft in-situ measurements (open star)(f) surface PM$_{2.5}$ and RH.). The vertical bars denote the periods

660   of flight profiles, with blue, black and red representing the clean period, transition period and heavy

661   pollution during a pollution event respectively. The other two pollution events can refer to supplement

662   Fig. S2 and Fig. S3.
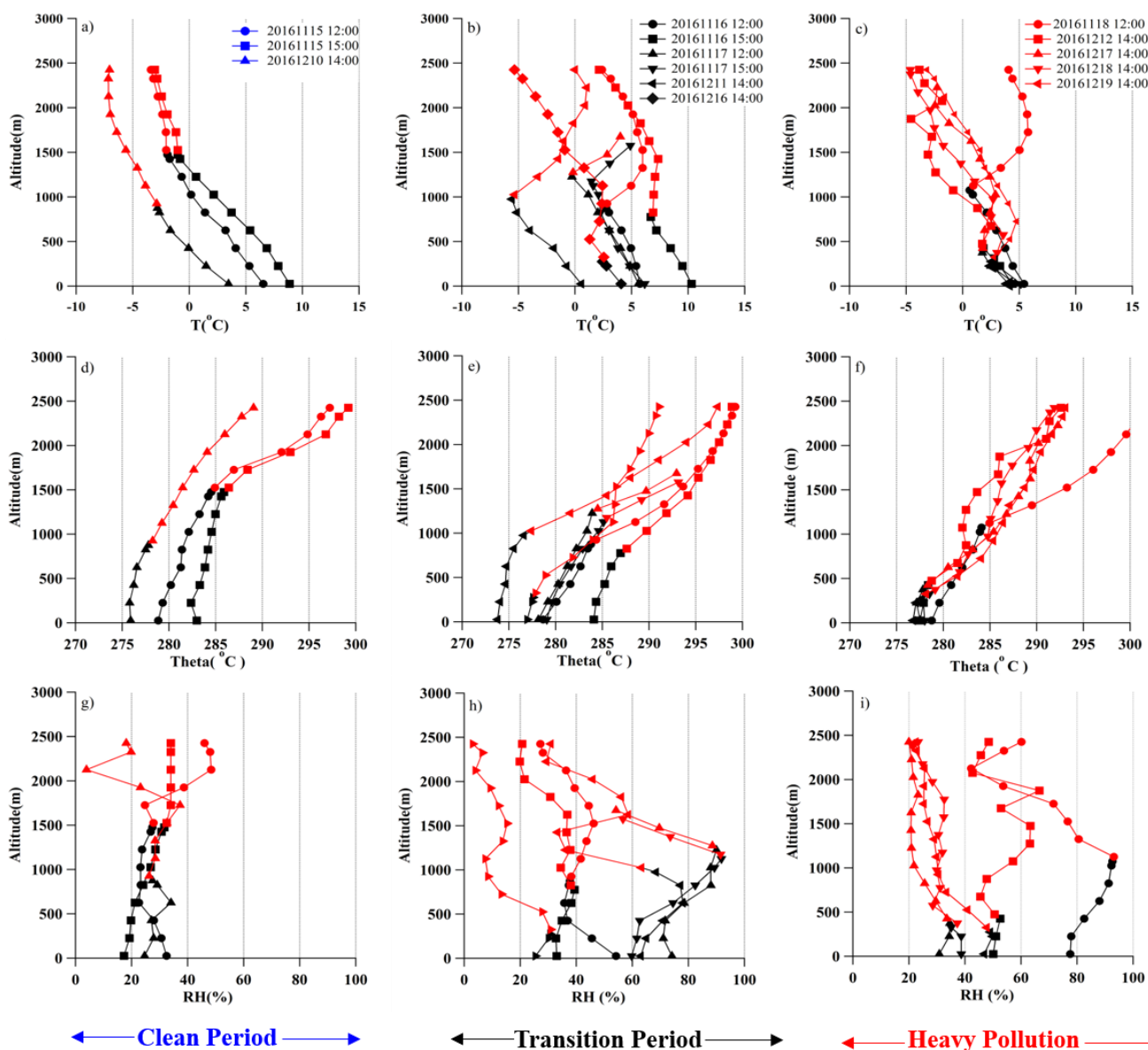
663
664   Fig. 2. Vertical profiles of temperature (a, b, c), relative humidity (d, e, f) and potential temperature (g,

665   h, i) for Clean Period, Transition Period and Heavy Pollution   period, respectively. The black and red

666   dots represent for inside the PBL and above the PBL.

667
668
669
670
671
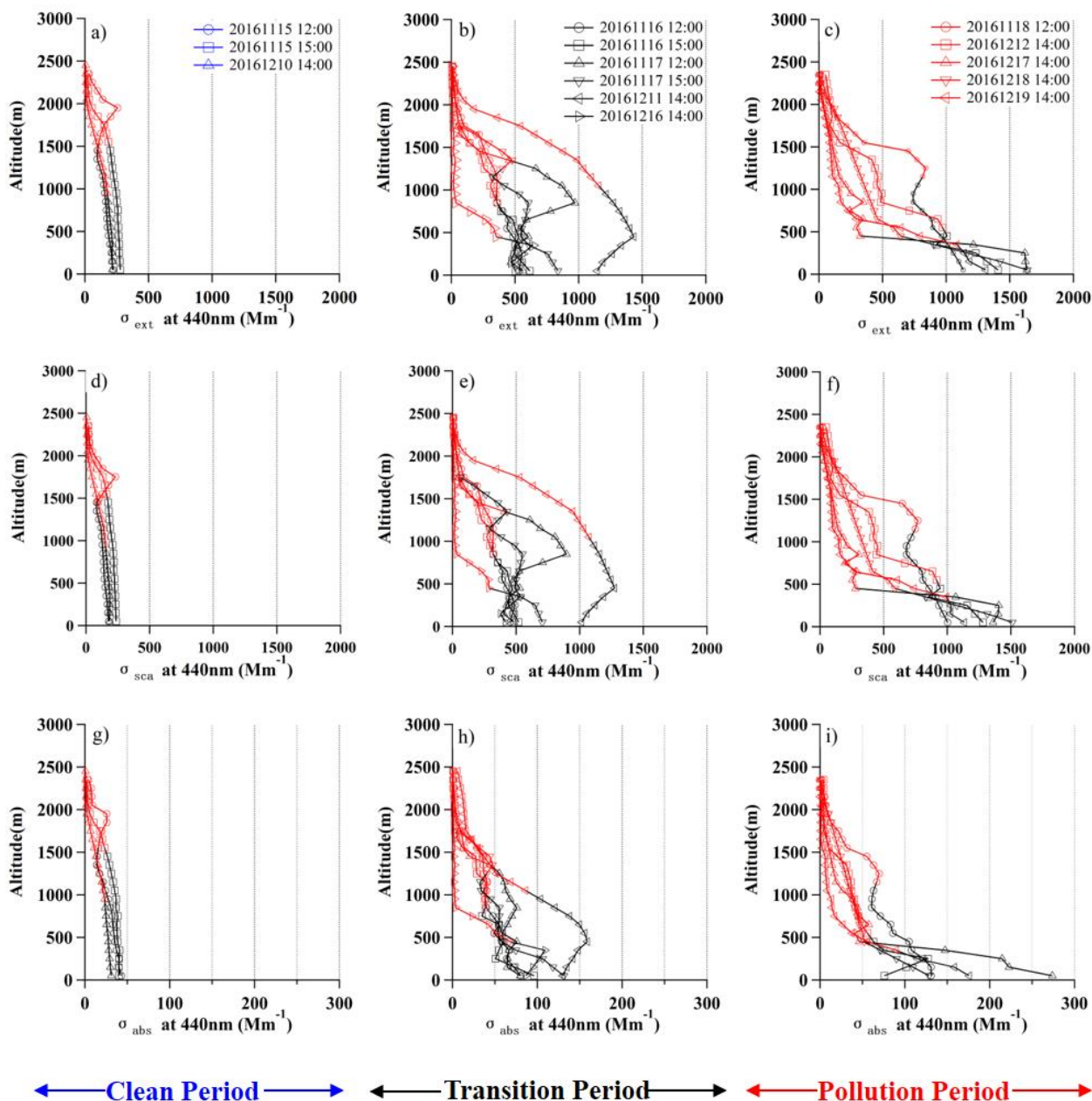
Fig. 3. Vertical profiles of aerosol extinction, scattering and absorption coefficient at 440 nm for CP

674 (blue), TP (black) and HP period (red), respectively. The blue and red lines represent for inside and

675 above the ML, respectively.

676

677
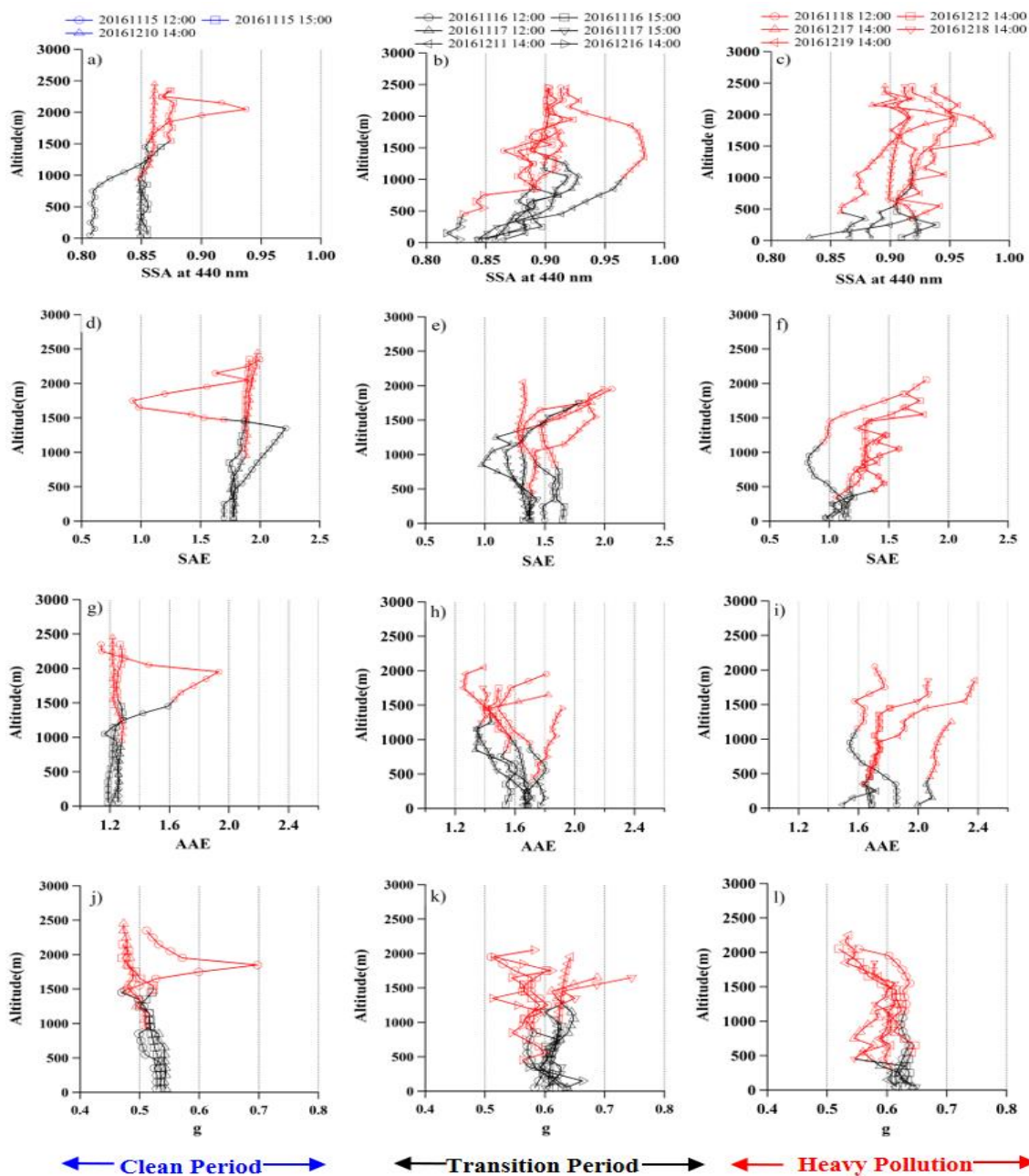
678

679 Fig. 4. Vertical profiles of aerosol single scattering albedo at 440 nm (SSA, a - c), scattering Angström

680 exponent (SAE, d - f), absorption Ångström exponent (AAE, g - i), and asymmetry parameter (g, j - l)

681 for CP (left panel), TP (middle panel) and HP period (right panel), respectively.
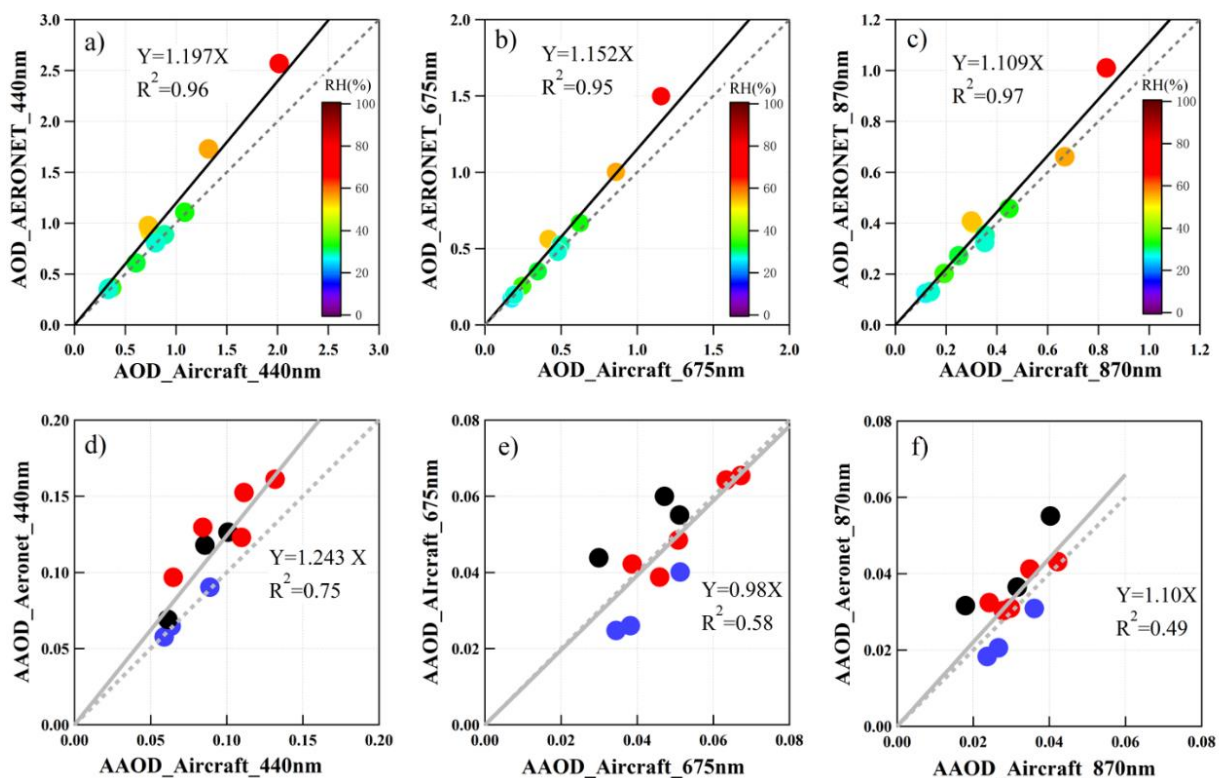
683 Fig. 5. Comparison between AERONET and aircraft in-situ constrained AOD and AAOD: a) - c) The

684 comparison of AOD between AERONET vs Aircraft at 440nm, 675nm, and 870nm, respectively, and

685 colored by RH; d) – f) Compare of AAOD between the retrieval AERONET one and aircraft in-situ

686 measurement at 440nm, 670nm, and 880nm. The blue, black, and red nots represent for CP, TP, and HP

687 period, respectively.

698
699
700
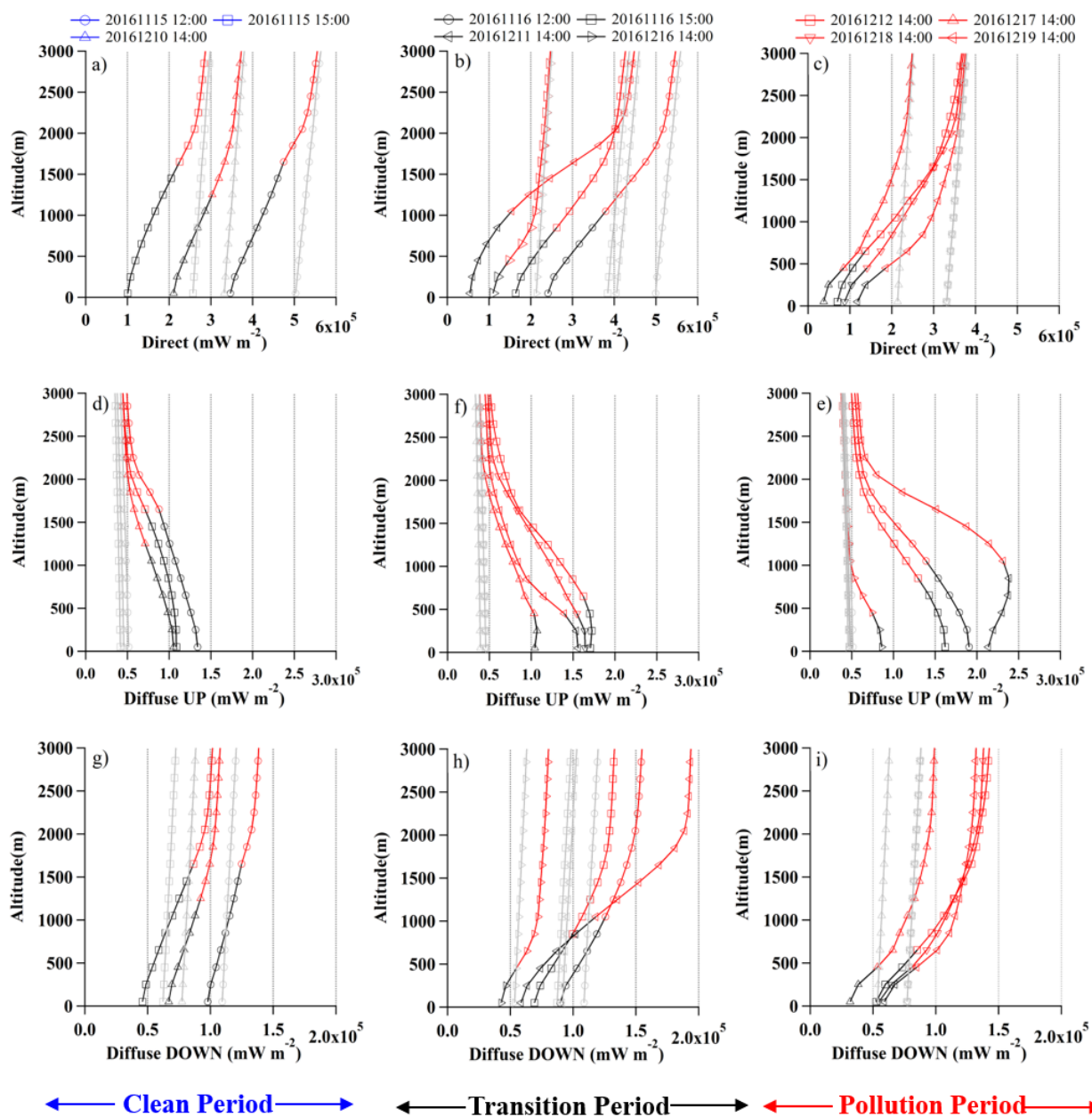
701
Fig. 6. Radiative transfer results calculated by DISTORT. a)-c), b)-e), and g)-i) show the direct, diffuse
702
703 upward and diffuse downward irradiance respectively. The left, middle and right panel represent for CP,
704 TP and HP period respectively, with black and red lines denoting above and within the PBL. The solid

line represent for the aerosol condition, while the grey dash line represent for the no-aerosol condition.
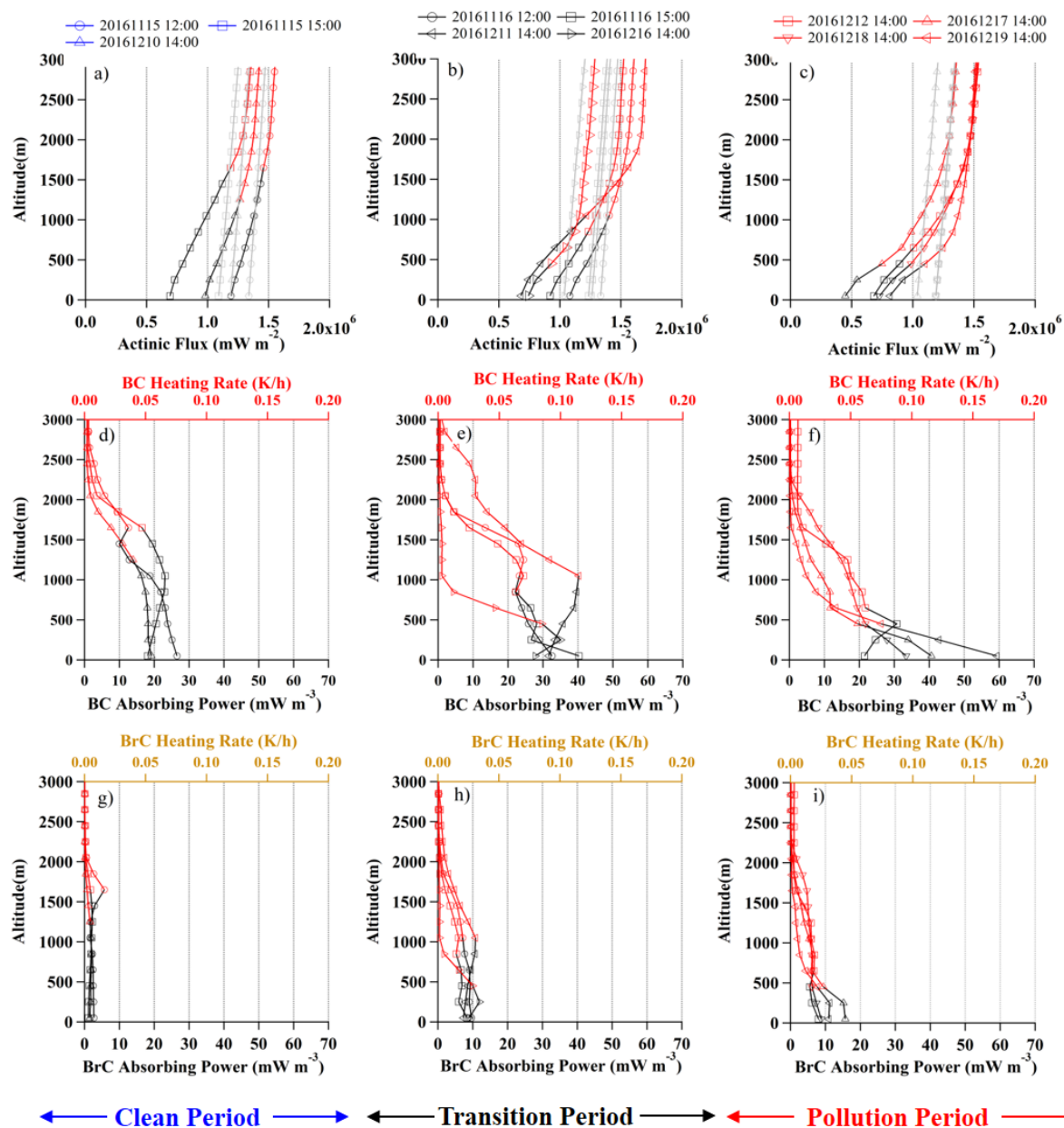
Fig. 7. Actinic flux (a-c), BC absorbing power (d-f) and BrC absorbing power (g-i). The left, middle and right panel was for LP, TP and HP respectively, with the black and red line denoting within and above the PBL. The gray lines in a) to c) show the aerosol free results. The upper x-axis from d) to i) shows the heating rate.

712
713

714
715 Fig. 8. Spectral absorption coefficient of BC and BrC inside and above the PBL for CP (a, d), TP (b, e)

716 and HP period (c, f), respectively, shown in black and brown carbon color respectively. The vertical

717 profiles of heating portion of BrC for CP, TP and HP period are shown in g) – i).
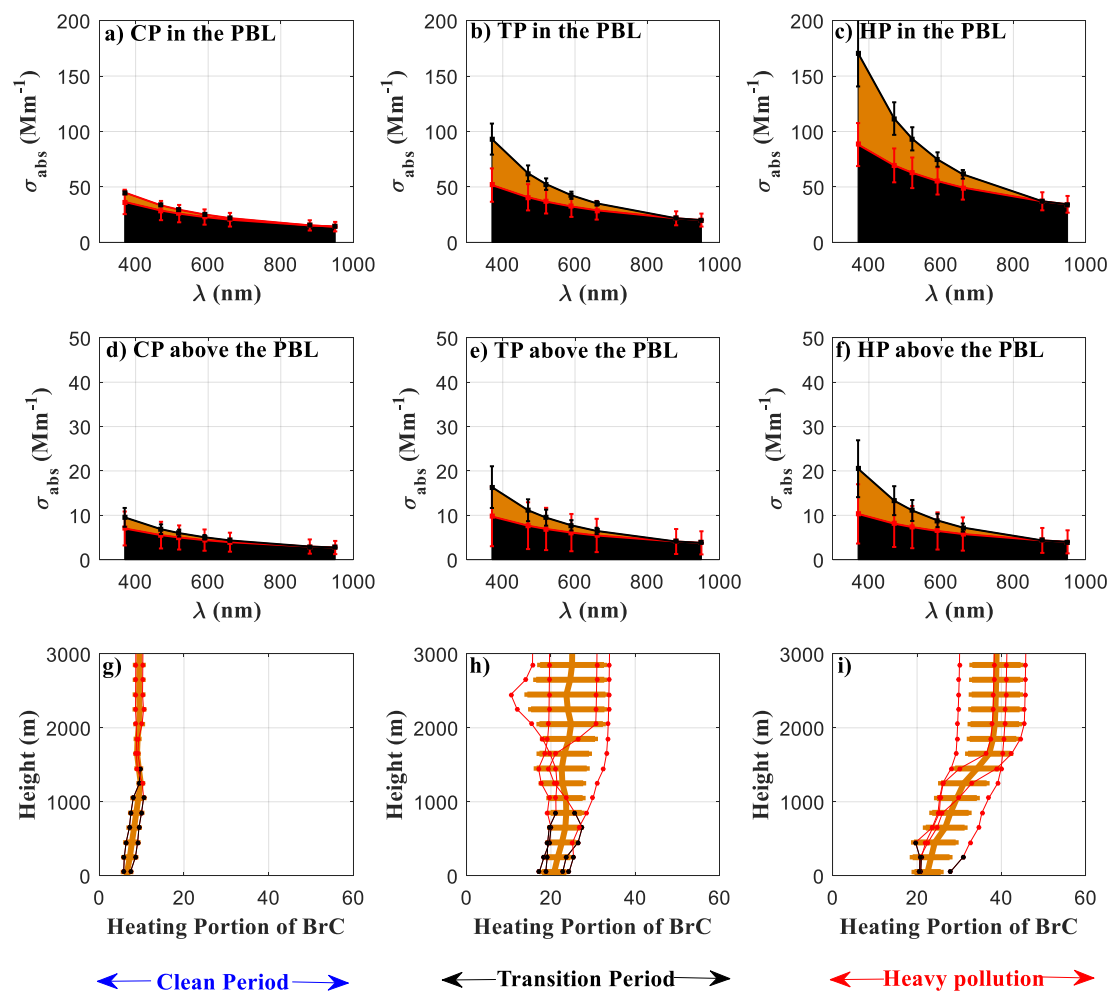
718
719
720
721
722
723
724